

Detecting Failures in Planar Phased Arrays: a Bayesian Compressive Sensing Approach

M. Salucci, A. Gelmini, G. Oliveri, and A. Massa

Abstract

In this work, the detection of failures in planar phased antenna arrays is dealt with. Towards this goal, the inverse problem at hand is formulated within a probabilistic framework and it is efficiently solved through a Bayesian compressive sensing (*BCS*) method. More in detail, starting from the knowledge of the failure-free (i.e., "gold") pattern and of that radiated by the antenna under test (*AUT*), the reconstruction of the faulty radiators is seen as a sparse retrieval problem whose solution does not require the compliance of the restricted isometry property (*RIP*) by the measurement operator. Some preliminary numerical results are shown to assess the effectiveness of the proposed array diagnosis tool.

Contents

1 Mathematical Formulation	2
2 Calibration of the <i>BCS</i> Diagnosis Method	6
2.1 Parameters	6
2.2 Results	8
3 Preliminary Assessment: Analysis vs. Array Failure Rate	9
3.1 Parameters	9
3.2 Results	11

1 Mathematical Formulation

Let us consider a planar array of N elements located in $\mathbf{r}_n = (x_n, y_n)$, $n = 1, \dots, N$ (Fig. 1).

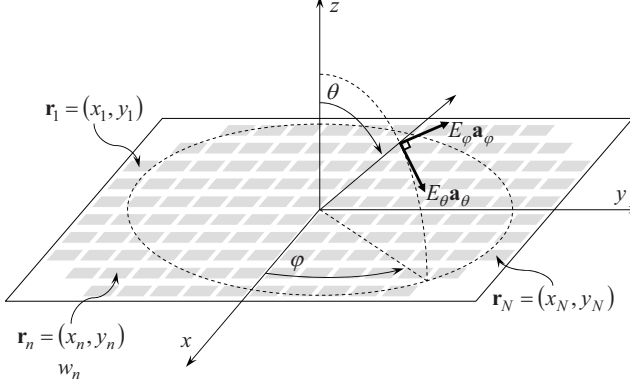


Figure 1: Geometry of the ideal planar array (*gold array*).

The far-field pattern radiated by the *failure-free* antenna (denoted in the following as the *gold array*) is given by

$$\mathbf{E}(u, v) = E_\theta(u, v) \mathbf{a}_\theta + E_\varphi(u, v) \mathbf{a}_\varphi \quad (1)$$

where \mathbf{a}_θ and \mathbf{a}_φ are the spherical unit vectors, $E_{\theta/\varphi}$ is the electric field component along $\mathbf{a}_{\theta/\varphi}$, while $u = \sin \theta \cos \varphi$ and $v = \sin \theta \sin \varphi$ are direction cosines (Fig. 1). Assuming that $\mathbf{E}(u, v)$ is known at K sampling directions (u_k, v_k) , $k = 1, \dots, K$, the samples of each q -th pattern component in (1) (i.e., $\underline{E}_q = \{E_q(u_k, v_k); k = 1, \dots, K\}$, $q = \{\theta; \varphi\}$) are related to the *gold array* excitations $\underline{w} = \{w_n \in \mathbb{C}; n = 1, \dots, N\}$ by means of the following expression

$$\underline{E}_q = \underline{\underline{G}}_q \underline{w}; \quad q = \{\theta; \varphi\}. \quad (2)$$

In (2) $\underline{\underline{G}}_q$ is the $(K \times N)$ “measurement matrix” for the q -th field component, whose (k, n) -th entry is defined as

$$G_{q,kn} = F_q^{(n)}(u_k, v_k) e^{j \frac{2\pi}{\lambda} (x_n u_k + y_n v_k)} \quad (3)$$

$$k = 1, \dots, K; n = 1, \dots, N; q = \{\theta; \varphi\}$$

λ being the free-space wavelength at the working frequency, while $F_q^{(n)}(u_k, v_k)$, $k = 1, \dots, K$, are samples of the q -th component ($q = \{\theta; \varphi\}$) of the n -th *embedded* element pattern

$$\mathbf{F}^{(n)}(u, v) = F_\theta^{(n)}(u, v) \mathbf{a}_\theta + F_\varphi^{(n)}(u, v) \mathbf{a}_\varphi \quad (4)$$

$$n = 1, \dots, N.$$

More precisely, each $\mathbf{F}^{(n)}(u, v)$ ($n = 1, \dots, N$) corresponds to the far-field pattern radiated by the planar arrangement when setting its excitations to

$$w_p = \begin{cases} 1 & \text{if } p = n \\ 0 & \text{otherwise} \end{cases}; \quad p = 1, \dots, N \quad (5)$$

and loading all $(N - 1)$ zero-excitation elements by the generator impedance¹. It is worth pointing out that in case of *real* elementary radiators Eq. (2) provides an *exact* representation of the radiated far-field. As a matter of fact, the patterns $\mathbf{F}^{(n)}(u, v)$, $n = 1, \dots, N$, do not only model the radiation behavior of the considered antennas (e.g., dipoles, patches, etc.), but they also describe all the effects of radiative mutual coupling (*MC*).

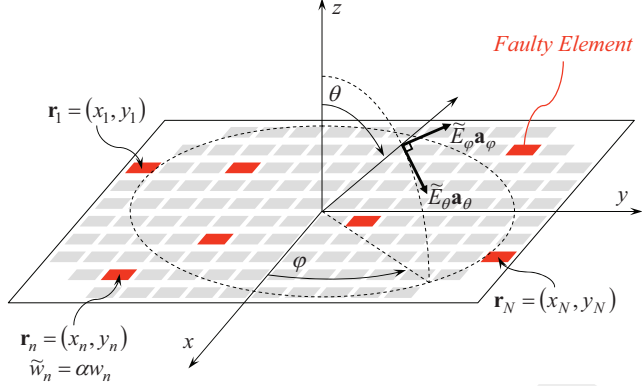


Figure 2: Geometry of the antenna under test (*AUT*).

Let us now consider that a small subset of $N_f = \Phi N \ll N$ elements ($0\% < \Phi << 100\%$ being the array *failure rate*) of the antenna under test (*AUT*) is failed (Fig. 2). Accordingly, indicating with $\tilde{\underline{w}} = \{\tilde{w}_n \in \mathbb{C}; n = 1, \dots, N\}$ the *AUT* excitations, it turns out that

$$\tilde{\underline{w}} = \text{diag}(\underline{\chi}) \underline{w} \quad (6)$$

where the entries of $\underline{\chi} = \{\chi_n; n = 1, \dots, N\}$ are equal to $\chi_n = \kappa$ whether the n -th element is damaged [κ being the antenna *failure factor* describing a total ($\kappa = 0 \rightarrow \tilde{w}_n = 0$) or a partial ($0 < \kappa < 1 \rightarrow \tilde{w}_n < w_n$) failure], $\chi_n = 1$ otherwise (i.e., for the $(N - N_f)$ healthy radiators). Accordingly, since $\tilde{\underline{w}} \neq \underline{w}$ for N_f entries, a deviation of the *AUT* far-field behavior from that of the *gold array* is observed, the (noisy) measured *AUT* pattern samples being equal to

$$\tilde{\underline{E}}_q = \underline{\underline{G}}_q \tilde{\underline{w}} + \underline{\underline{H}}_q; \quad q = \{\theta; \varphi\} \quad (7)$$

where $\tilde{\underline{E}}_q = \{\tilde{E}_q(u_k, v_k); k = 1, \dots, K\}$, while $\underline{\underline{H}}_q = \{H_q(u_k, v_k); k = 1, \dots, K\}$ contains the samples of an additive zero-mean Gaussian noise. Under these hypotheses, it is possible to define the *differential pattern* samples

$$\begin{aligned} \Delta \underline{E}_q &= \{\Delta E_q(u_k, v_k); k = 1, \dots, K\} = \\ &= (\underline{\underline{E}}_q - \tilde{\underline{E}}_q) = \underline{\underline{G}}_q \underline{d} - \underline{\underline{H}}_q; \quad q = \{\theta; \varphi\} \end{aligned} \quad (8)$$

corresponding to the far-field distribution generated by a fictitious *differential antenna* (Fig. 3) excited by the set of complex coefficients

$$\underline{d} = \{d_n = (w_n - \tilde{w}_n); n = 1, \dots, N\}. \quad (9)$$

¹A local coordinate system centered on \mathbf{r}_n is considered in the definition of each n -th embedded element pattern $\mathbf{F}^{(n)}(u, v)$ in (4), for $n = 1, \dots, N$.

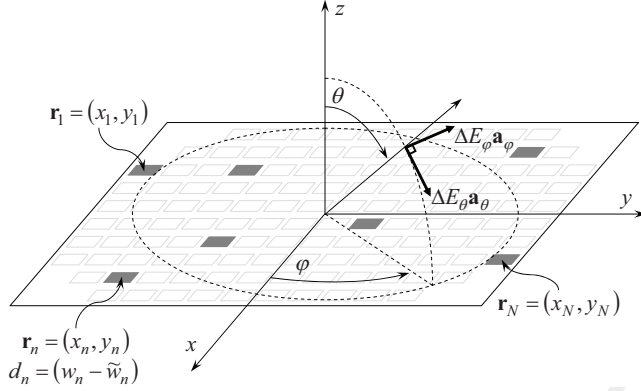


Figure 3: Geometry of the *differential* antenna.

It is worth observing that the *failure vector* $\underline{d} \in \mathbb{C}^N$ is intrinsically sparse since it is characterized by few non-null entries (i.e., those corresponding to the N_f failed radiators, for which $\tilde{w}_n \neq w_n \Rightarrow d_n \neq 0$), its ℓ_0 -norm being equal to $\|\underline{d}\|_0 = N_f \ll N$ [3]. Accordingly, it is possible to exploit such an *a-priori* information by formulating the planar array diagnosis problem as follows:

Planar Array Diagnosis Problem - Given the samples of the *differential pattern*, $\underline{\Delta E}_q$, $q = \{\theta; \varphi\}$, and of the *embedded* element patterns, $\underline{F}_q^{(n)} = \left\{ F_q^{(n)}(u_k, v_k); k = 1, \dots, K \right\}$, $n = 1, \dots, N$, $q = \{\theta; \varphi\}$, retrieve the unknown set \underline{d} complying with

$$\underline{\underline{G}}_q \underline{d} - \underline{\Delta E}_q = \underline{H}_q; \quad q = \{\theta; \varphi\} \quad (10)$$

subject to \underline{d} is *sparse*.

Given the linear nature of (10) as well as the sparseness of the unknown, a *BCS* solution approach is exploited to effectively solve the problem at hand without requiring - unlike standard *CS*-based approaches [5][6] - any compliance of the *RIP* condition by the two matrix operators $\underline{\underline{G}}_{\theta/\varphi}$, as detailed in the following.

Since the applicability of available *BCS* solvers is limited to real-valued linear formulations, in order to solve the planar array diagnosis problem Eq. (10) is rearranged as follows

$$\underline{\underline{G}}_q \underline{\underline{\delta}} - \underline{\Psi}_q = \underline{\underline{H}}_q; \quad q = \{\theta; \varphi\} \quad (11)$$

where $\underline{\underline{\delta}} = [\Re\{\underline{d}\}, \Im\{\underline{d}\}]^T \in \mathbb{R}^{2N}$ comprises the real (i.e., $\Re\{\underline{d}\} = [\Re\{d_n\}; n = 1, \dots, N]$) and imaginary ($\Im\{\underline{d}\} = [\Im\{d_n\}; n = 1, \dots, N]$) parts of the unknown vector \underline{d} , while $\underline{\Psi}_q = [\Re\{\underline{\Delta E}_q\}, \Im\{\underline{\Delta E}_q\}]^T \in \mathbb{R}^{2K}$, $\underline{\underline{H}}_q = [\Re\{\underline{H}_q\}, \Im\{\underline{H}_q\}]^T \in \mathbb{R}^{2K}$, and

$$\underline{\underline{G}}_q = \begin{bmatrix} \Re\{\underline{\underline{G}}_q\} & -\Im\{\underline{\underline{G}}_q\} \\ \Im\{\underline{\underline{G}}_q\} & \Re\{\underline{\underline{G}}_q\} \end{bmatrix} \in \mathbb{R}^{2K \times 2N}; \quad q = \{\theta; \varphi\} \quad (12)$$

$.^T$ being the transpose operator. Accordingly, the problem at hand is formulated within the Bayesian framework, retrieving an estimation of $\underline{\delta}$ as follows

$$\hat{\underline{\delta}} = \frac{1}{2} \sum_{q=\{\theta; \varphi\}} \left\{ \frac{1}{\hat{\sigma}_q^2} \left[\frac{\underline{\mathcal{G}}_q^T \underline{\mathcal{G}}_q}{\hat{\sigma}_q^2} + \text{diag}(\hat{\underline{\zeta}}_q) \right]^{-1} \underline{\mathcal{G}}_q^T \underline{\Psi}_q \right\} \quad (13)$$

where $\hat{\sigma}_q^2$ and $\hat{\underline{\zeta}}_q = \{\hat{\zeta}_{q,n}; n = 1, \dots, 2N\}$ are respectively the estimated noise variance and the set of *BCS* hyper-parameters, determined by maximizing through a fast relevance vector machine (*RVM*) solver the *BCS marginal likelihood* function

$$\mathcal{L}^{ST-BCS}(\sigma_q^2, \underline{\zeta}_q) = -\frac{1}{2} \left[2K \log 2\pi + \log |\underline{\mathcal{W}}_q| + \underline{\Psi}_q^T \underline{\mathcal{W}}_q^{-1} \underline{\Psi}_q \right] \quad (14)$$

where

$$\underline{\mathcal{W}}_q = \sigma_q^2 + \underline{\mathcal{G}}_q \left[\text{diag}(\underline{\zeta}_q) \right]^{-1} \underline{\mathcal{G}}_q^T. \quad (15)$$

Finally, the set of complex retrieved failures $\hat{\underline{d}} = \{\hat{d}_n; n = 1, \dots, N\}$ is derived from (13) by letting

$$\hat{d}_n = (\hat{\delta}_n + j\hat{\delta}_{n+N}); \quad n = 1, \dots, N. \quad (16)$$

It is worth pointing out that the posterior probability $\mathcal{P}(\underline{\delta}|\underline{\Psi}_q)$ is modelled as a multi-variate normal distribution $\mathcal{N}(\underline{\mu}_q, \underline{\mathcal{S}}_q)$ with mean vector $\underline{\mu}_q = \sigma_q^{-2} \underline{\mathcal{S}}_q \underline{\mathcal{G}}_q^T \underline{\Psi}_q$ and co-variance matrix

$$\underline{\mathcal{S}}_q = \left[\text{diag}(\underline{\zeta}_q) + \sigma_q^{-2} \underline{\mathcal{G}}_q \underline{\mathcal{G}}_q^T \right]^{-1}. \quad (17)$$

Accordingly, $\underline{\mathcal{S}}_q$ provides useful information about the *confidence* of the *BCS* diagnosis, since its diagonal entries, $S_{q,nn}$, are inversely proportional to the degree of *reliability* of $\hat{\delta}_n$, for $n = 1, \dots, 2N$. Consequently, it is possible to compute the *total confidence* of the *BCS* solution as

$$\Gamma = \frac{1}{4N} \sum_{q=\{\theta; \varphi\}} \sum_{n=1}^{2N} (S_{q,nn})^2 \quad (18)$$

lower values of Γ indicating a higher *reliability* of the *BCS* diagnosis.

2 Calibration of the BCS Diagnosis Method

The goal of this Section is the calibration of the main parameters of the developed diagnosis method, i.e.,

1. The noise variance initialization value, η ;
2. The ratio between measurements and number of elements in the array: $\nu = \frac{K}{N}$.

Throughout the whole numerical analysis, the “quality” of the array diagnosis will be quantitatively measured in terms of the normalized diagnosis error, defined as follows [3]

$$\xi = 100 \times \frac{1}{I} \sum_{i=1}^I \left[\frac{\sum_{n=1}^N |d_n^{(i)} - \hat{d}_n^{(i)}|^2}{\sum_{n=1}^N |d_n^{(i)}|^2} \right] \quad (19)$$

where the apex i denotes the i -th ($i = 1, \dots, I$; $I = 100$) realization of the process of randomly locating a fixed set of N_f failures (i.e., a value of the failure rate Φ) within the AUT.

2.1 Parameters

- Gold array

- Total number of elements: $N = 316$;
- Type of elements: isotropic/ideal²
- Spacing along x and y : $d_x = d_y = 0.5 [\lambda]$;
- Excitation tapering: Taylor;
 - * Radius: $R = 5 [\lambda]$;
 - * Transition index: $t = 3$;
 - * Peak sidelobe level: $PSL = 25 [\text{dB}]$

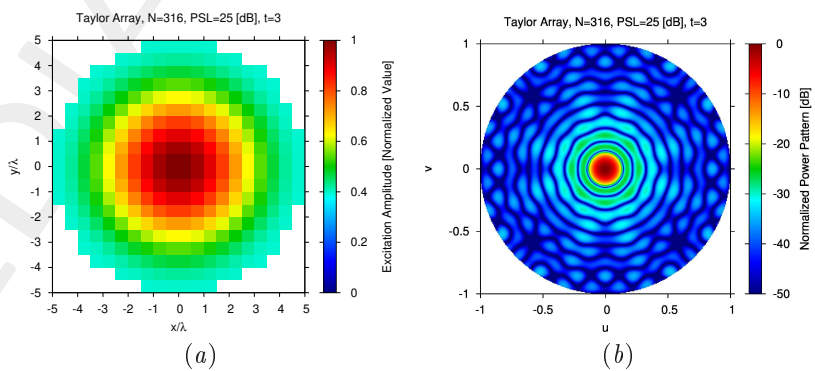


Figure 4: Sensitivity Analysis (Taylor Array, $N = 316$, $PSL = 25 [\text{dB}]$, $t = 3$) - (a) Array excitations and (b) normalized power pattern of the expected array (gold antenna).

²In order to model *isotropic* radiators, let us assume that in (4) the embedded elements patterns are equal to $F_\theta^{(n)}(u, v) = 1$ and $F_\varphi^{(n)}(u, v) = 0$, for $n = 1, \dots, N$.

- Failed Array

- Number of failures: $N_f = 13$;
- Failure rate: $\Phi = \frac{N_f}{N} \simeq 4\%$;
- Failure factor: $\kappa = 0$ (total failures);

- Measurement set-up

- Type of sampling: uniform sampling in the (u, v) plane;
- Number of points along u and v : see table below (calibrated parameter);

K_u	K_v	K	$\nu = \frac{K}{N}$
18	18	216	0.68
19	19	253	0.80
20	20	276	0.87
21	21	317	1.00
22	22	332	1.05

Table 1: Sensitivity Analysis (Taylor Array, $N = 316$, $PSL = 25$ [dB], $t = 3$) - Number of sampling points in $-1.0 \leq u \leq 1.0$ (K_u) and in $-1.0 \leq v \leq 1.0$ (K_v), total number of sampling points falling in the visible range (K), and ratio between measurements and number of elements ($\nu = \frac{K}{N}$).

- *BCS* solver

- Noise variance: $\eta = \{10^{-9}; 5 \times 10^{-9}; 10^{-8}; \dots; 10^1\}$ (calibrated parameter);
- Tolerance factor: $\iota = 10^{-8}$;
- Signal-to-Noise-Ratio: $SNR = \{20; 30; 40; 50; 60\}$.

2.2 Results

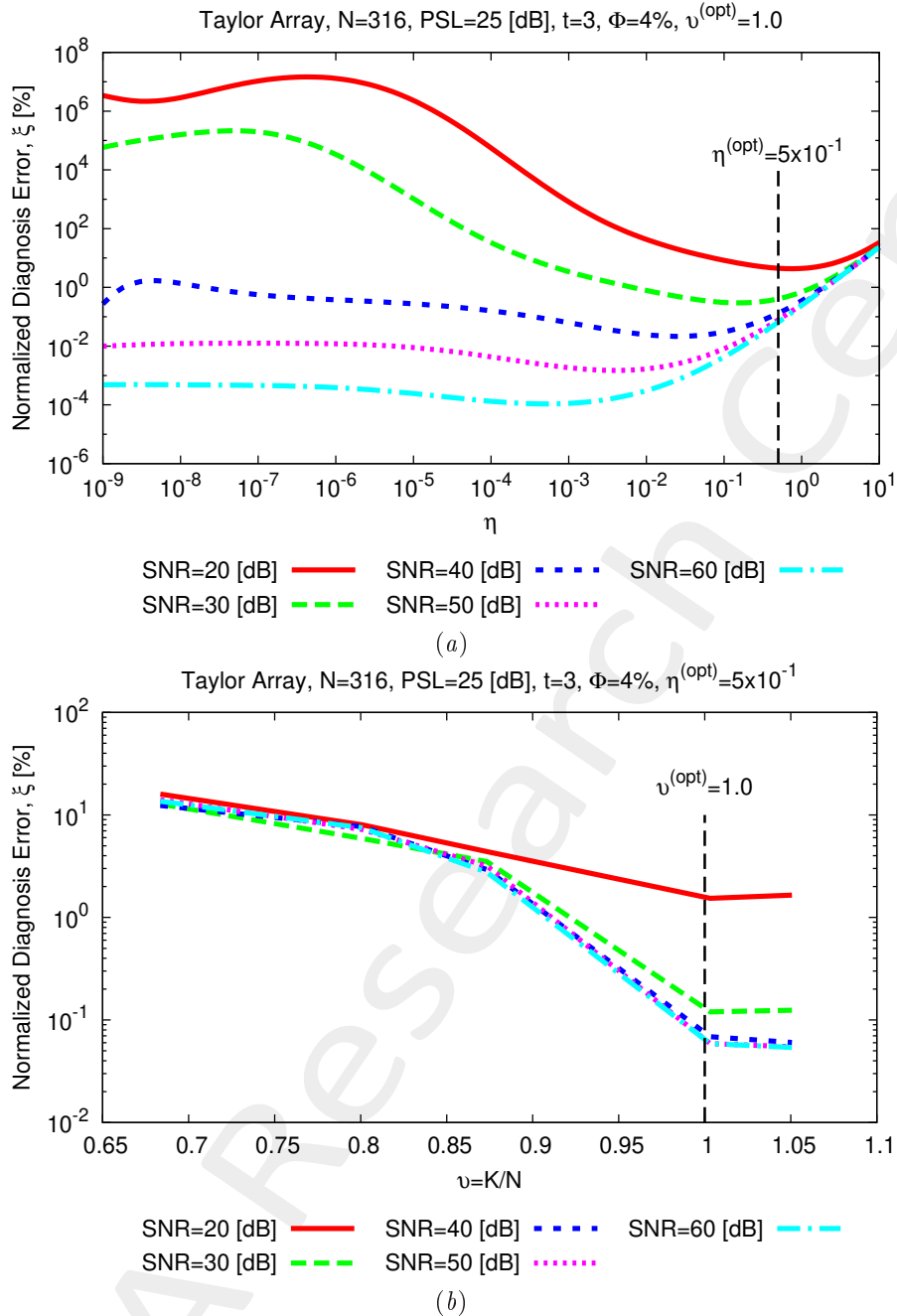


Figure 5: Sensitivity Analysis (Taylor Array, $N = 316$, $PSL = 25$ [dB], $t = 3$) - Behavior of the average diagnosis error versus (a) the BCS noise variance, η , and (b) the ratio $\nu = \frac{K}{N}$.

According to the obtained results, the optimal (η, ν) pair is

$$(\eta^{(opt)}, \nu^{(opt)}) = (5 \times 10^{-1}, 1.0) \quad (20)$$

Such a configuration will be considered for the successive numerical validations.

3 Preliminary Assessment: Analysis vs. Array Failure Rate

The purpose of this Section is to show a preliminary numerical assessment of the proposed *BCS* planar array diagnosis method. Towards this end, a variation of the number of failed elements (i.e., of the array failure factor, Φ) and of the *SNR* on measured far-field samples will be considered.

3.1 Parameters

- Gold array
 - Total number of elements: $N = 316$;
 - Type of elements: isotropic/ideal³
 - Spacing along x and y : $d_x = d_y = 0.5 [\lambda]$;
 - Excitation tapering: Taylor;
 - * Radius: $R = 5 [\lambda]$;
 - * Transition index: $t = 3$;
 - * Peak sidelobe level: $PSL = 25 [\text{dB}]$

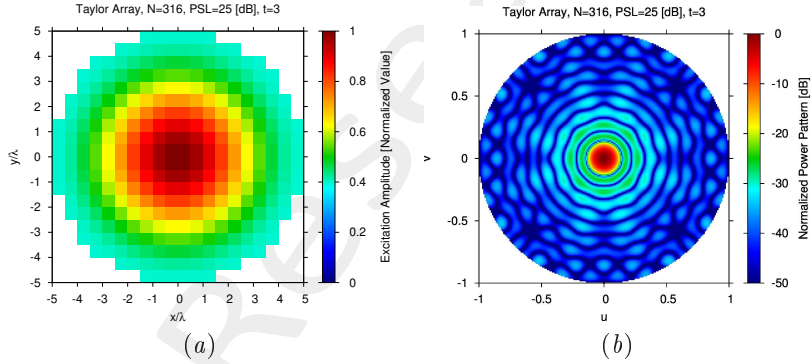


Figure 6: (a) Array excitations and (b) normalized power pattern of the expected array (gold antenna).

- Failed Array
 - Failure factor: $\kappa = 0$ (total failures);
 - Failure rate: see table below;

³In order to model *isotropic* radiators, let us assume that in (4) the embedded elements patterns are equal to $F_\theta^{(n)}(u, v) = 1$ and $F_\varphi^{(n)}(u, v) = 0$, for $n = 1, \dots, N$.

N_f	$\Phi = \frac{N_f}{N}$
3	1%
6	2%
13	4%
25	8%
32	10%
38	12%
51	16%
63	20%

Table 2: Number of failures (N_f) and corresponding failure rate ($\Phi = \frac{N_f}{N}$).

- Measurement set-up
 - Type of sampling: uniform sampling in the (u, v) plane;
 - Number of points along u and v : $K_u = K_v = 21$;
 - Number of points in the visible range: $K = 317$;
 - Ratio between measurements and number of elements: $\nu = \frac{K}{N} \simeq 1.0$ ($\nu^{(opt)}$);
- *BCS* solver
 - Noise variance: $\eta = 5 \times 10^{-1}$ ($\eta^{(opt)}$);
 - Tolerance factor: $\iota = 10^{-8}$;
- Signal-to-Noise-Ratio: $SNR = \{10; 20; \dots; 100\}$.

3.2 Results

$\Phi = \frac{N_f}{N} = 1\%$ ($N_f = 3$) - Best and Worst BCS Reconstructions

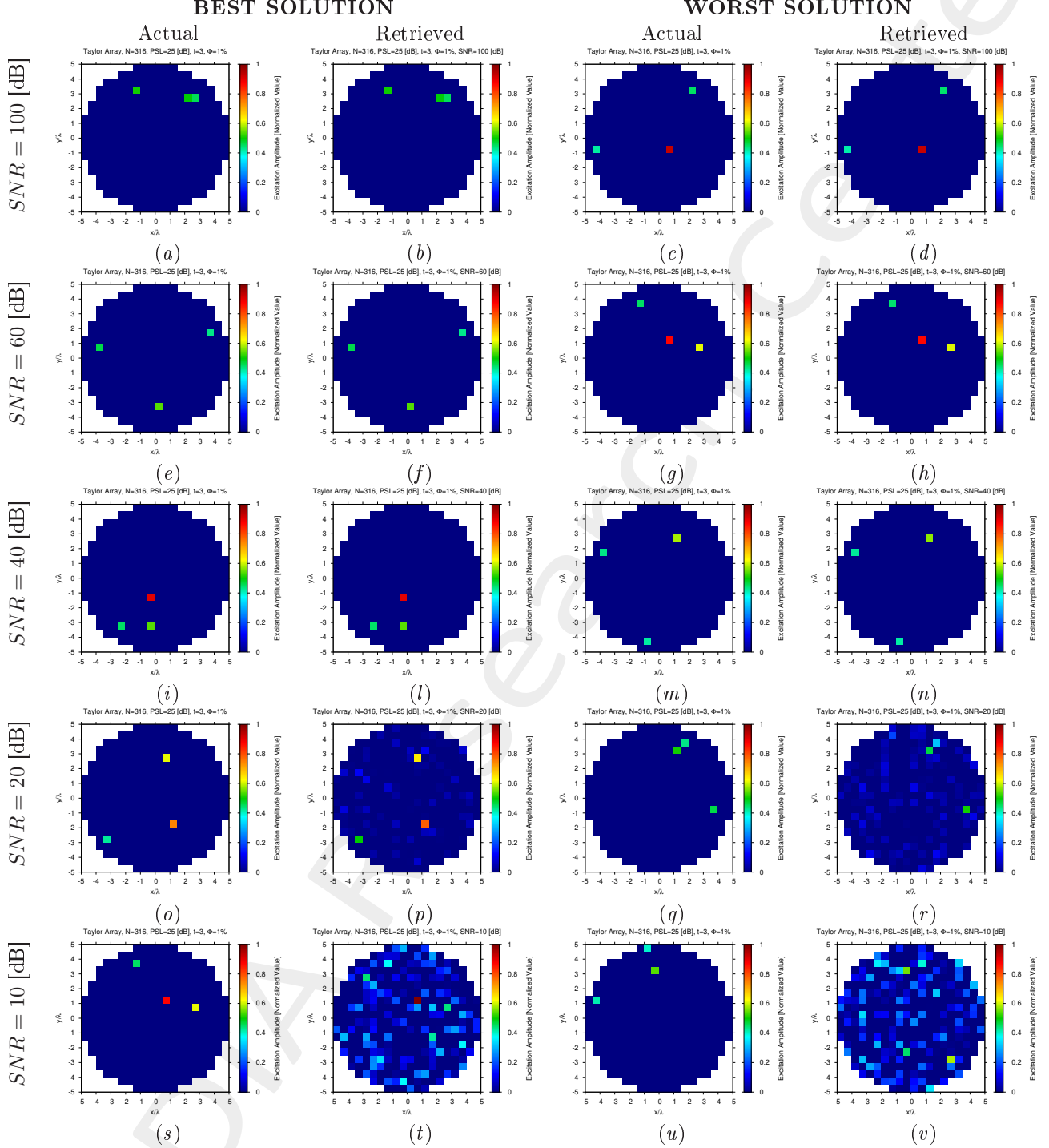


Figure 7: Taylor Array ($N = 316$, $PSL = 25$ [dB], $t = 3$, $\Phi = 1\%$) - Best and worst reconstructions under several SNR values.

$$\Phi = \frac{N_f}{N} = 2\% \quad (N_f = 6) - \text{Best and Worst BCS Reconstructions}$$

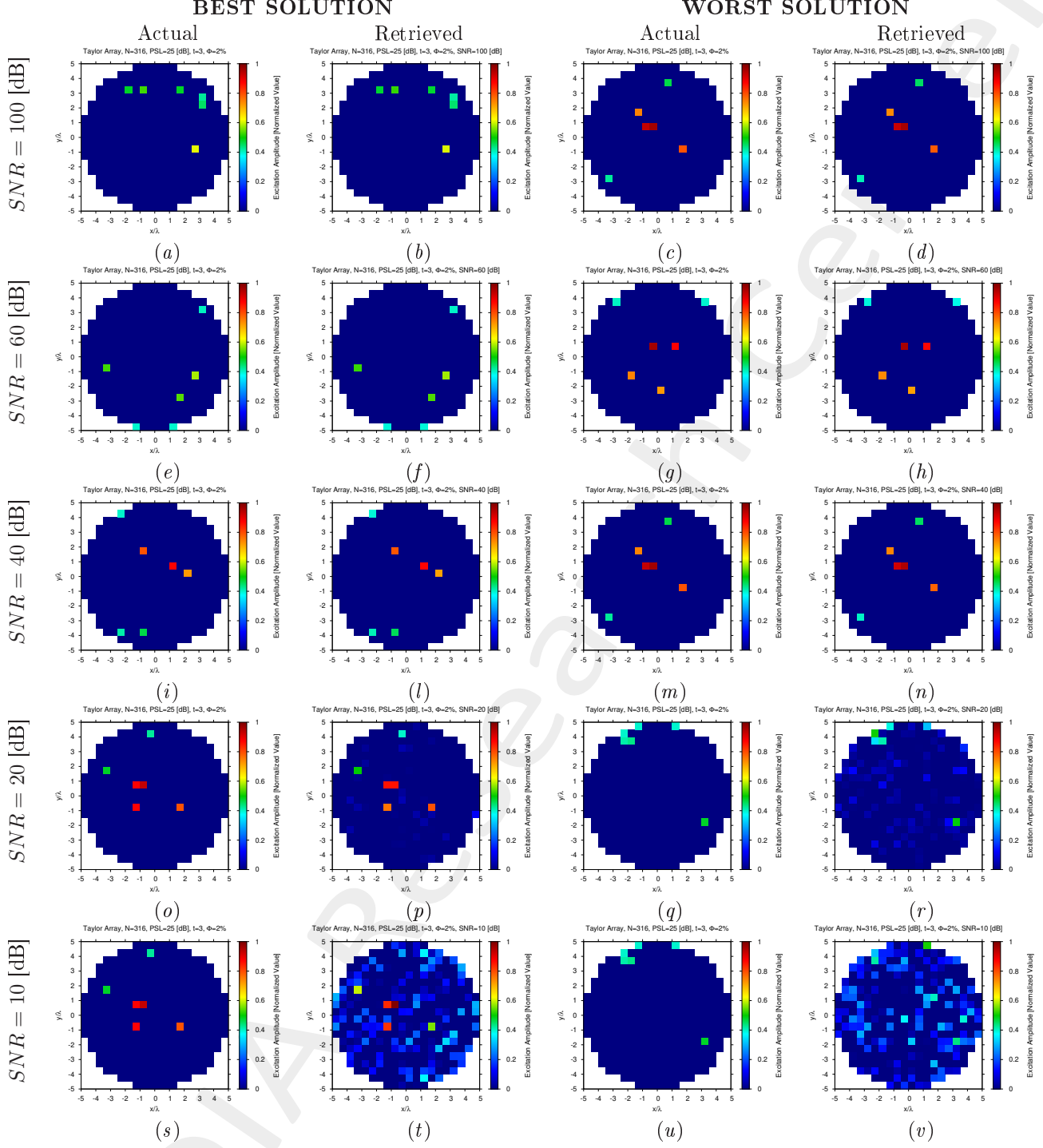


Figure 8: Taylor Array ($N = 316$, $PSL = 25$ [dB], $t = 3$, $\Phi = 2\%$) - Best and worst reconstructions under several SNR values.

$\Phi = \frac{N_f}{N} = 4\% \ (N_f = 13)$ - Best and Worst BCS Reconstructions

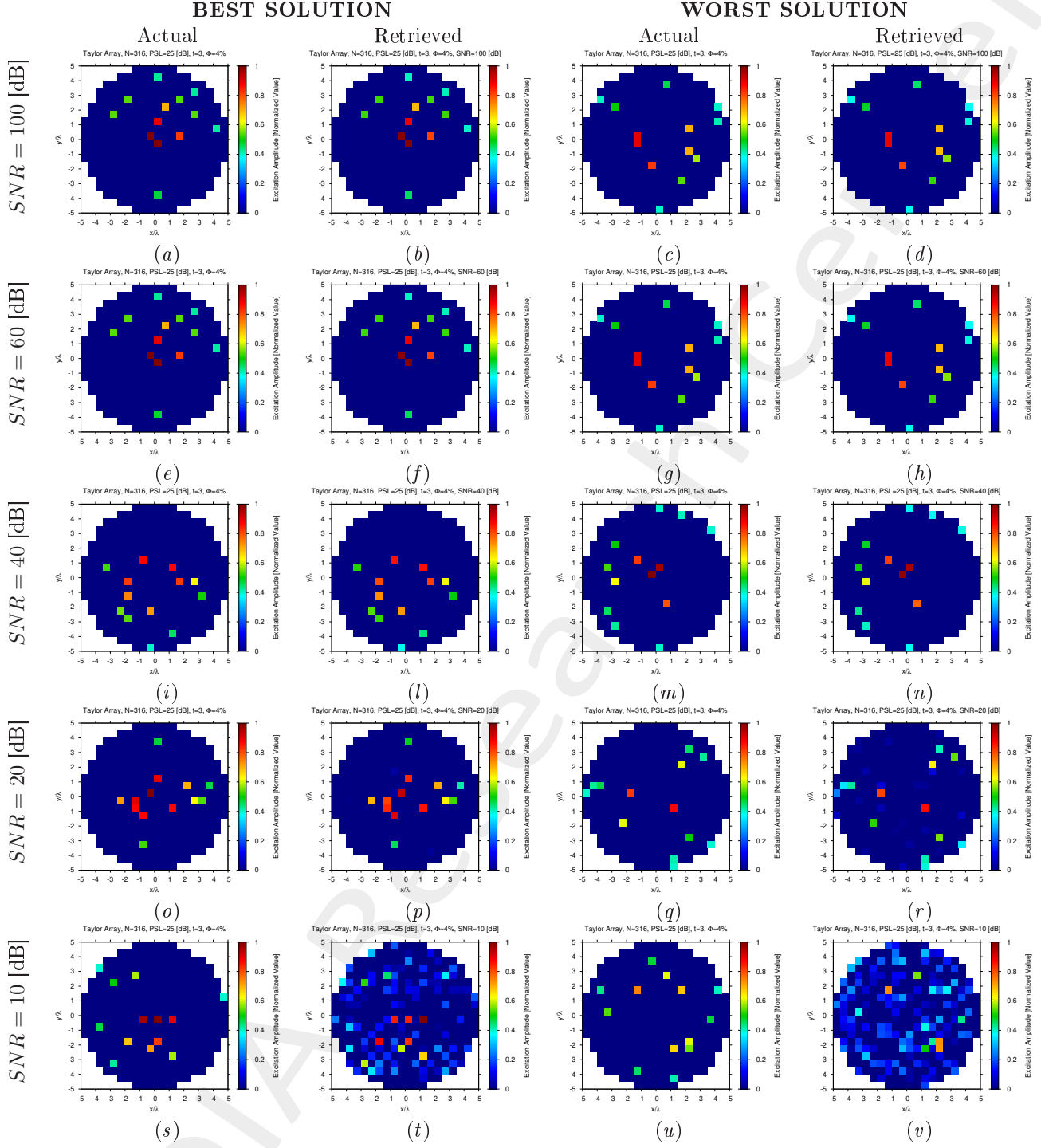


Figure 9: Taylor Array ($N = 316$, $PSL = 25 \ [\text{dB}]$, $t = 3$, $\Phi = 4\%$) - Best and worst reconstructions under several SNR values.

$\Phi = \frac{N_f}{N} = 8\% \ (N_f = 25)$ - Best and Worst BCS Reconstructions

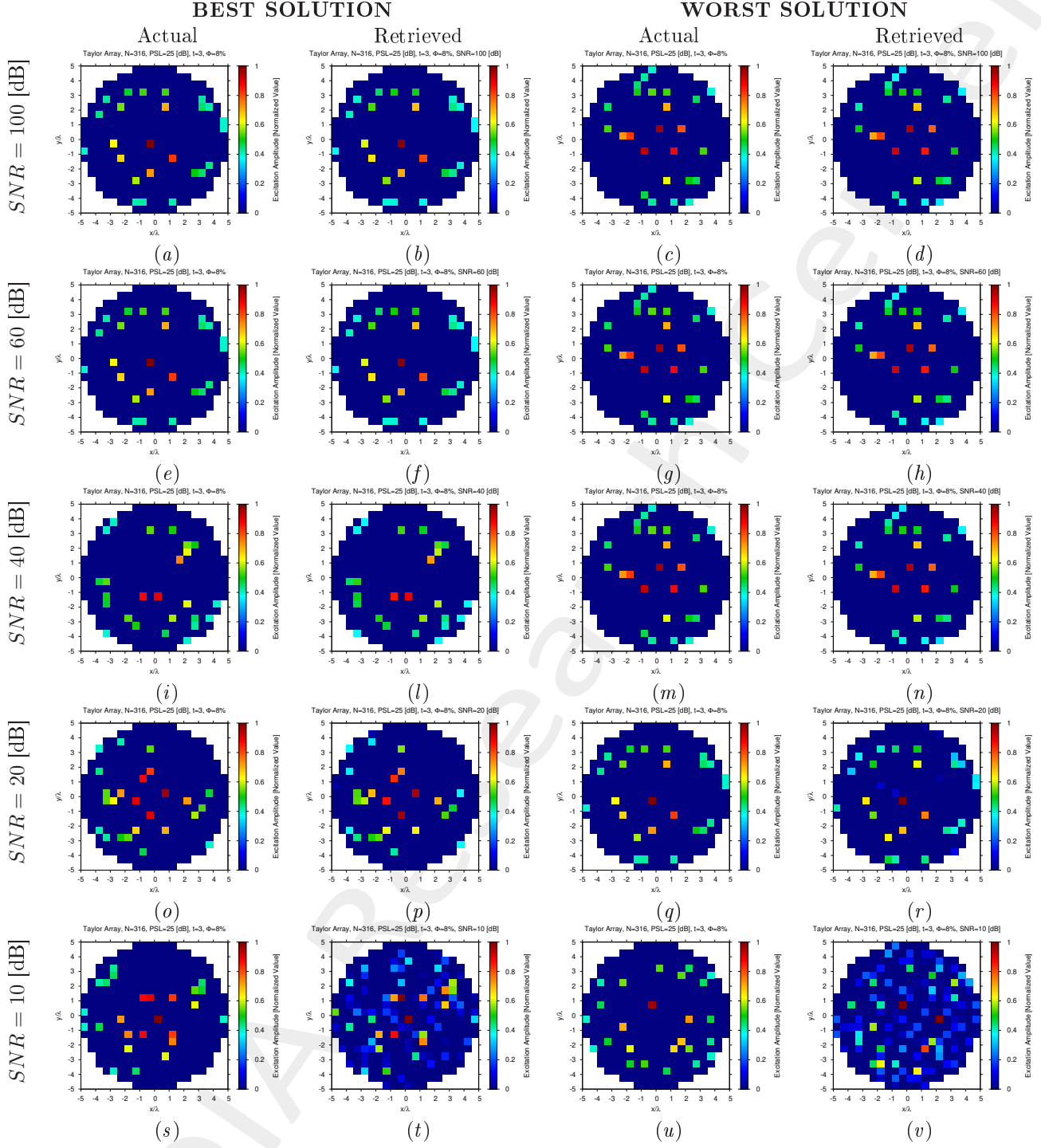


Figure 10: Taylor Array ($N = 316$, $PSL = 25 \ [\text{dB}]$, $t = 3$, $\Phi = 8\%$) - Best and worst reconstructions under several SNR values.

$\Phi = \frac{N_f}{N} = 10\%$ ($N_f = 32$) - Best and Worst BCS Reconstructions

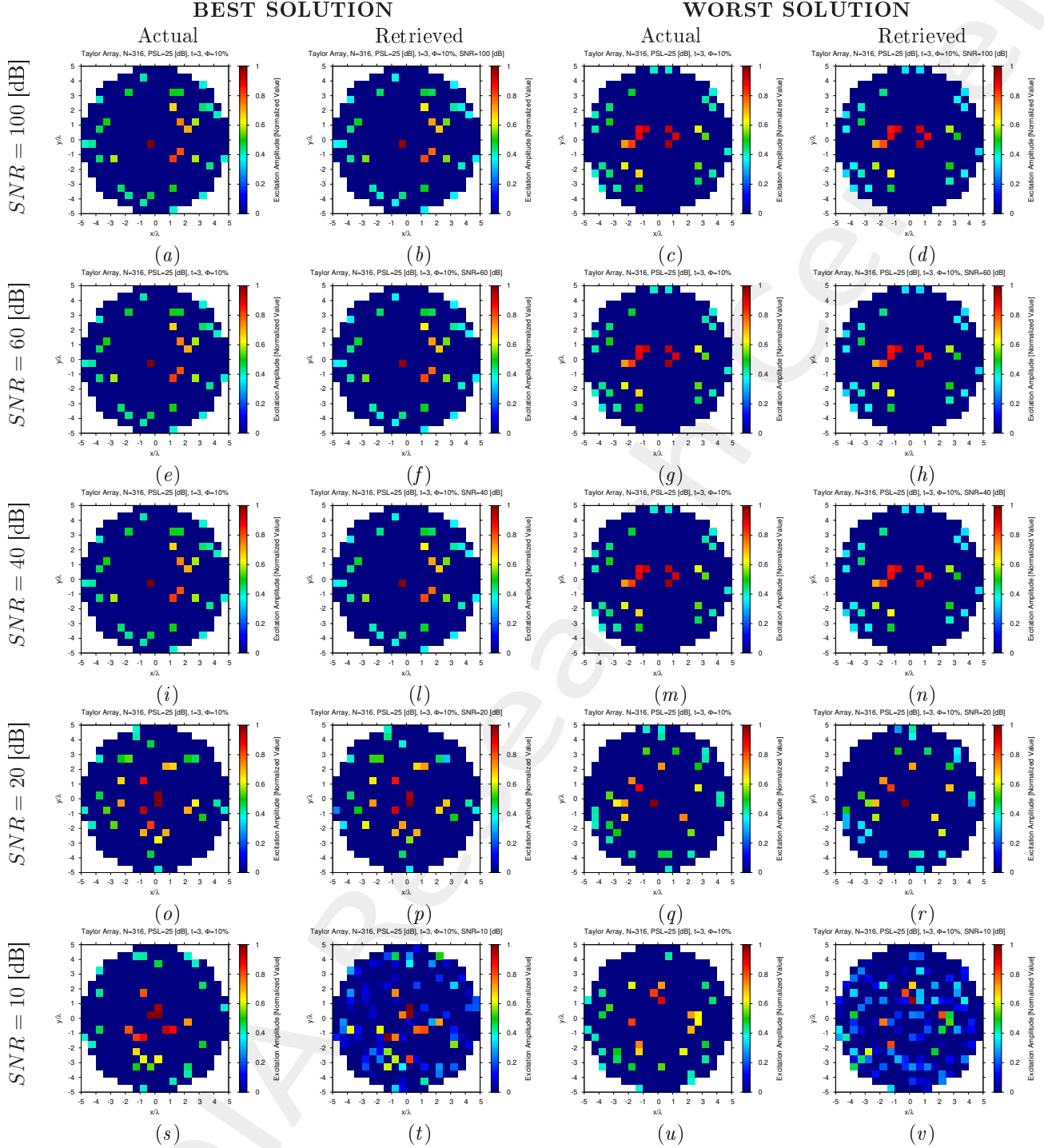


Figure 11: Taylor Array ($N = 316$, $PSL = 25$ [dB], $t = 3$, $\Phi = 10\%$) - Best and worst reconstructions under several SNR values.

$$\Phi = \frac{N_f}{N} = 12\% \quad (N_f = 38) - \text{Best and Worst BCS Reconstructions}$$

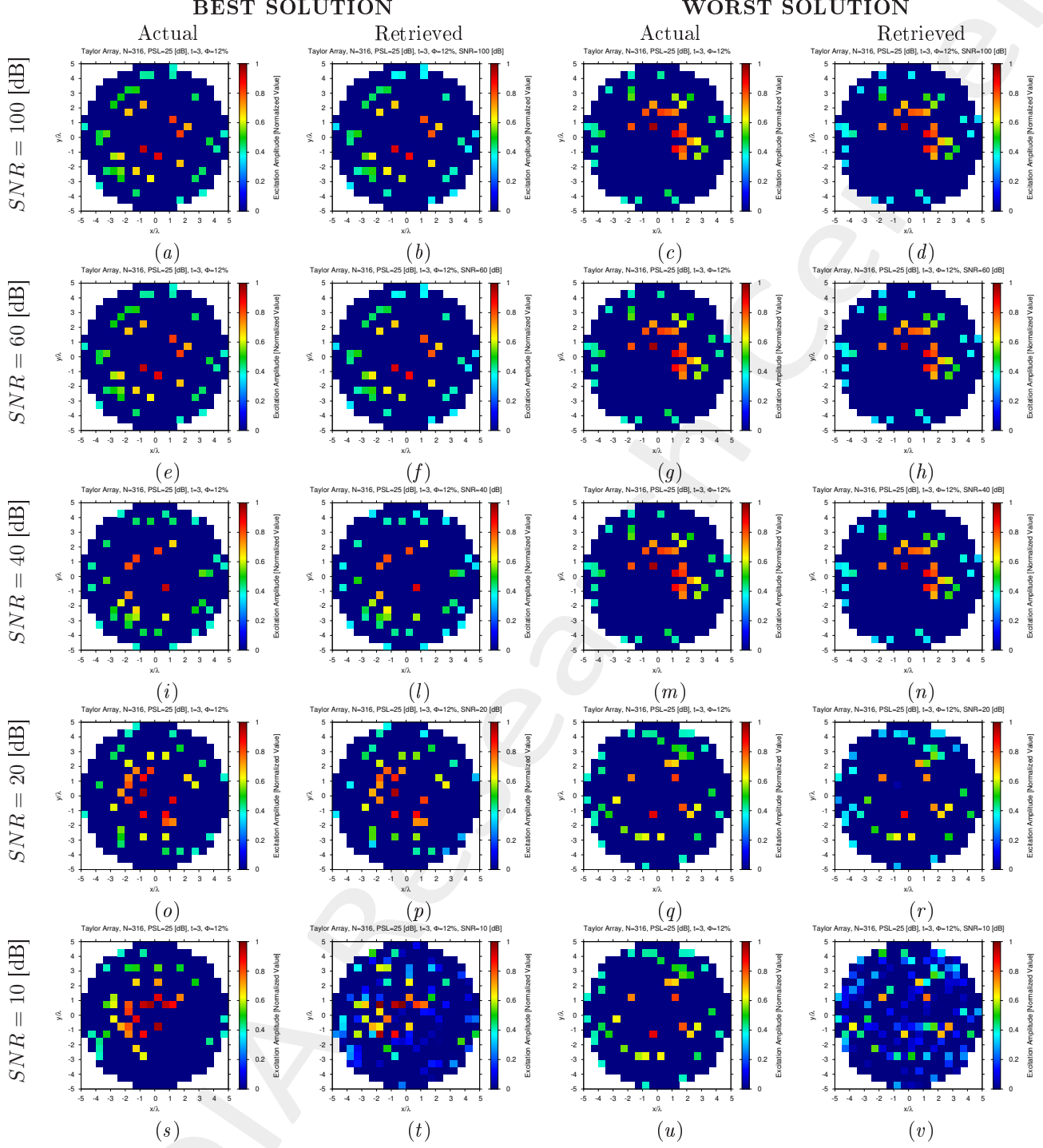


Figure 12: Taylor Array ($N = 316$, $PSL = 25$ [dB], $t = 3$, $\Phi = 12\%$) - Best and worst reconstructions under several SNR values.

$$\Phi = \frac{N_f}{N} = 16\% \quad (N_f = 51) - \text{Best and Worst BCS Reconstructions}$$

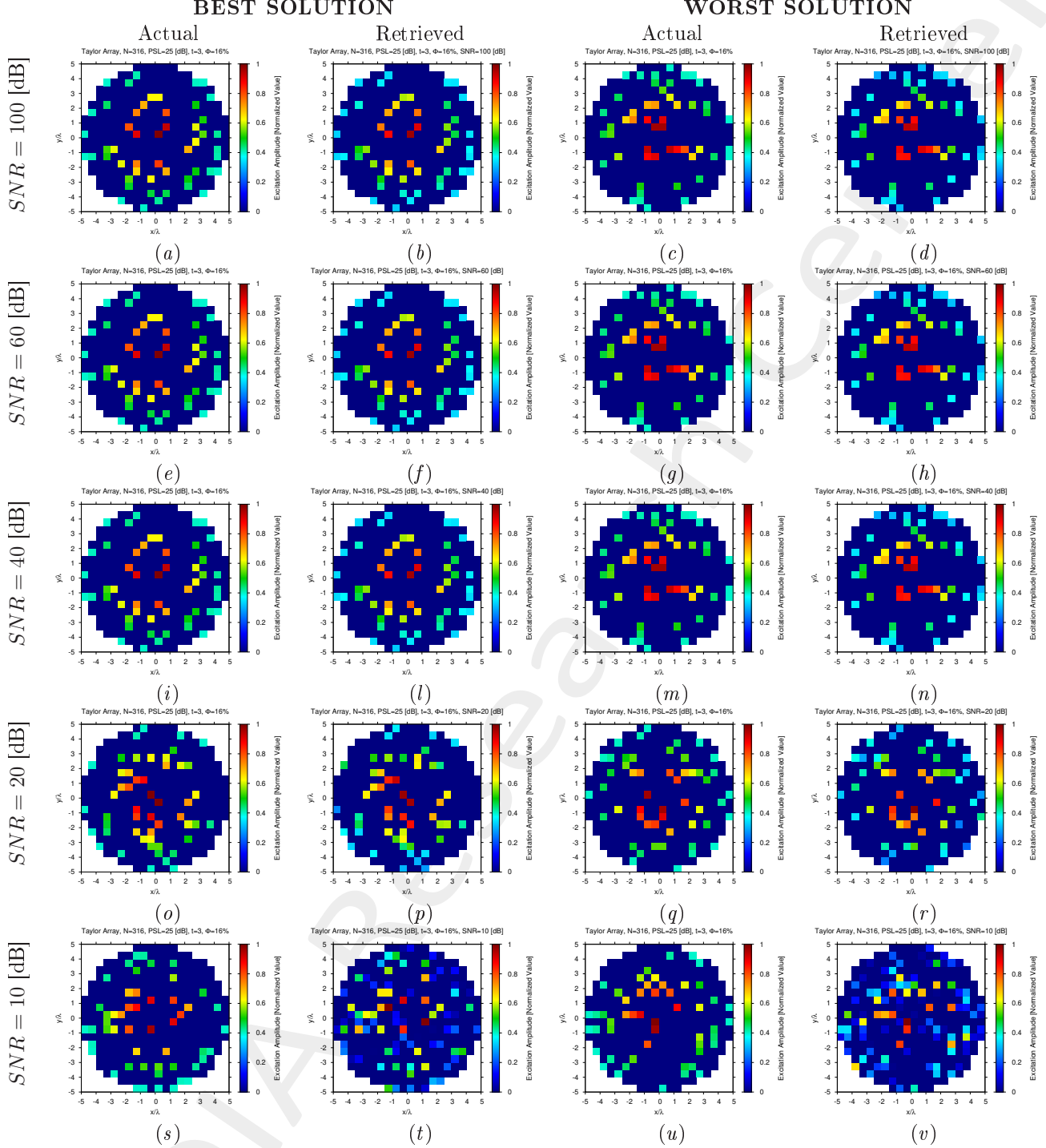


Figure 13: Taylor Array ($N = 316$, $PSL = 25$ [dB], $t = 3$, $\Phi = 16\%$) - Best and worst reconstructions under several SNR values.

$$\Phi = \frac{N_f}{N} = 20\% \quad (N_f = 63) - \text{Best and Worst BCS Reconstructions}$$

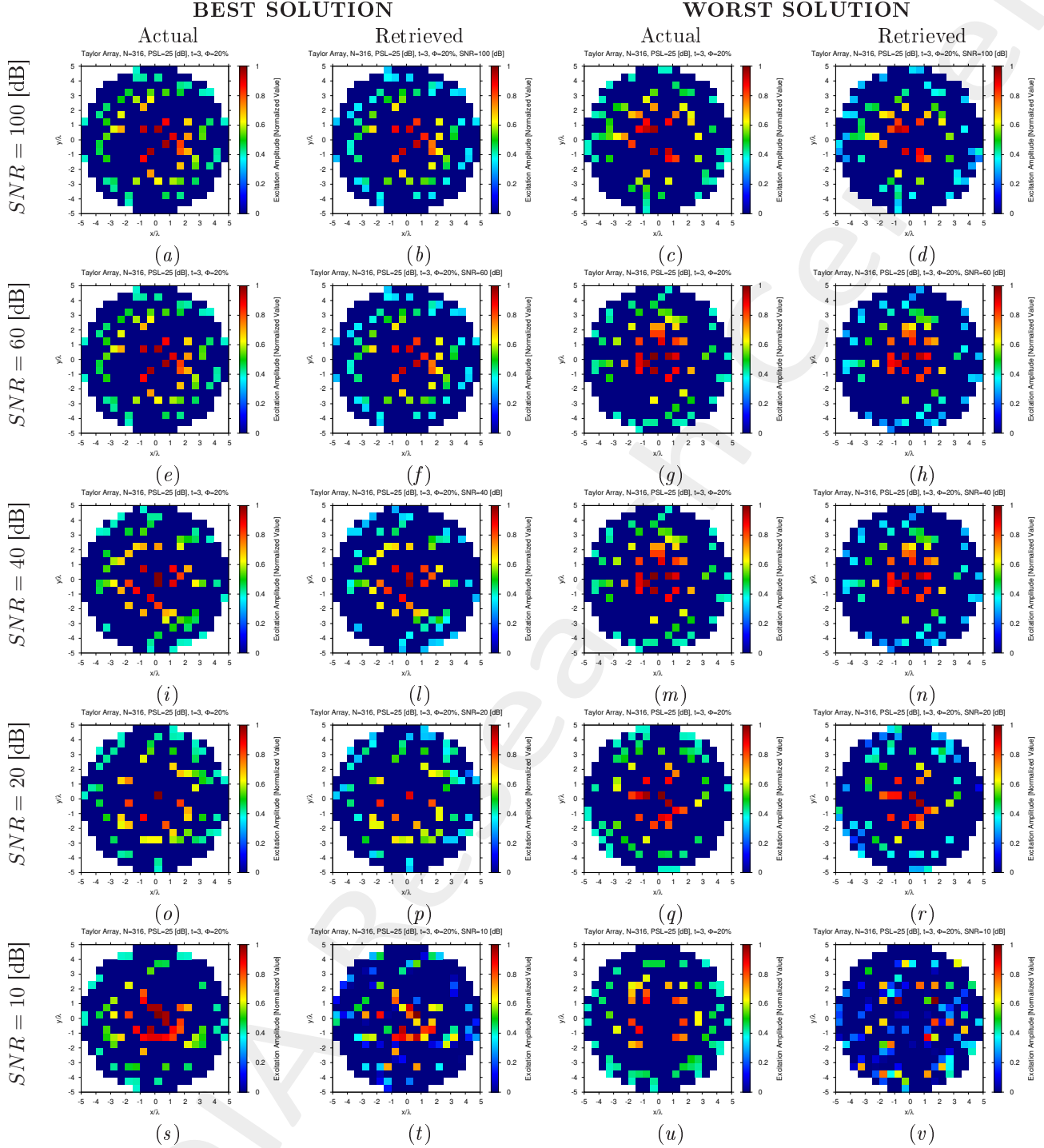


Figure 14: Taylor Array ($N = 316$, $PSL = 25$ [dB], $t = 3$, $\Phi = 20\%$) - Best and worst reconstructions under several SNR values.

Diagnosis Error and Confidence Level

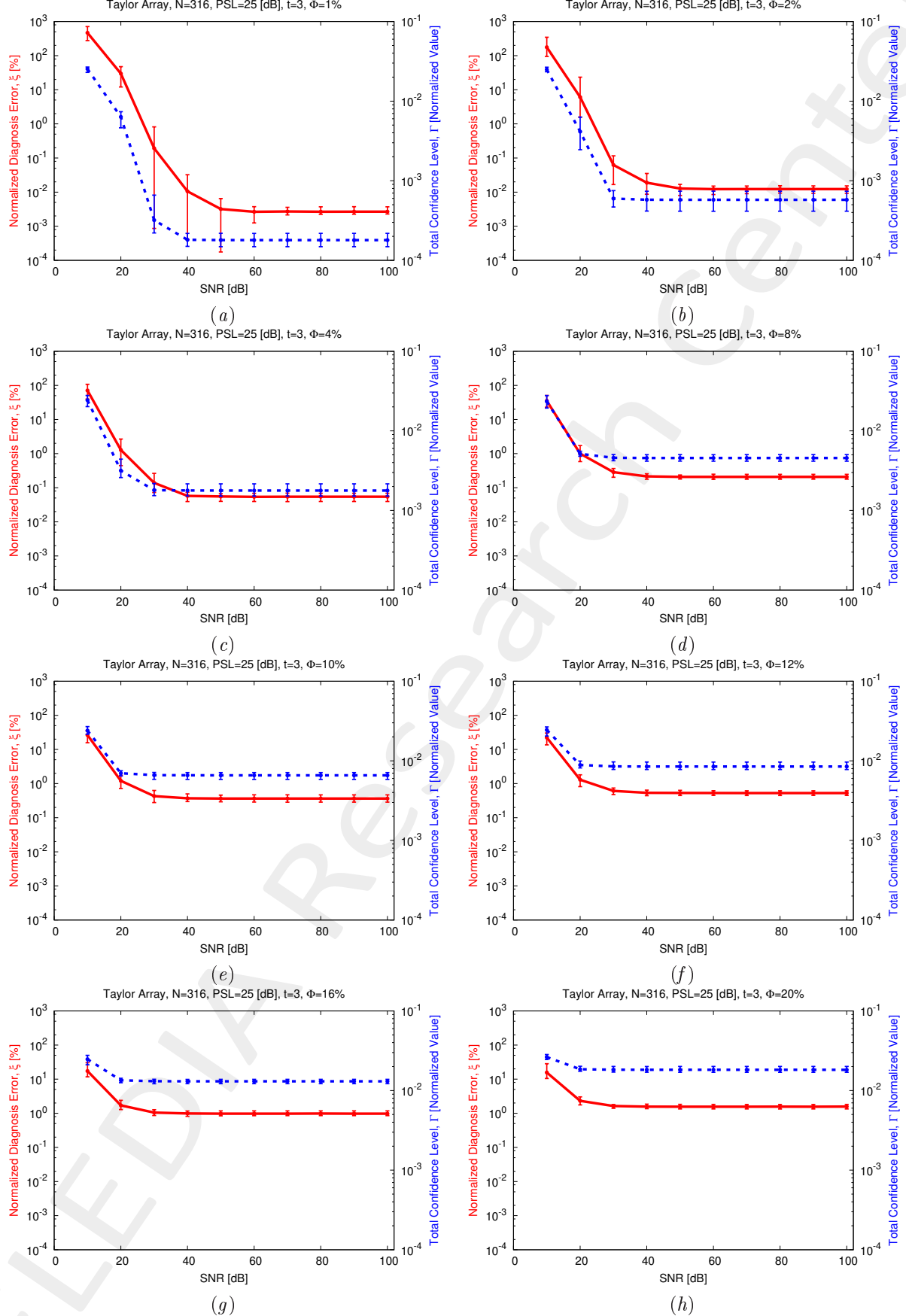


Figure 15: Taylor Array ($N = 316$, $PSL = 25$ dB, $t = 3$) - Behavior of the average, minimum and maximum diagnosis error (ξ) and total confidence level (Γ) versus the SNR , for (a) $\Phi = 1\%$, (b) $\Phi = 2\%$, (c) $\Phi = 4\%$, (d) $\Phi = 8\%$, (e) $\Phi = 10\%$, (f) $\Phi = 12\%$, (g) $\Phi = 16\%$, and (h) $\Phi = 20\%$.

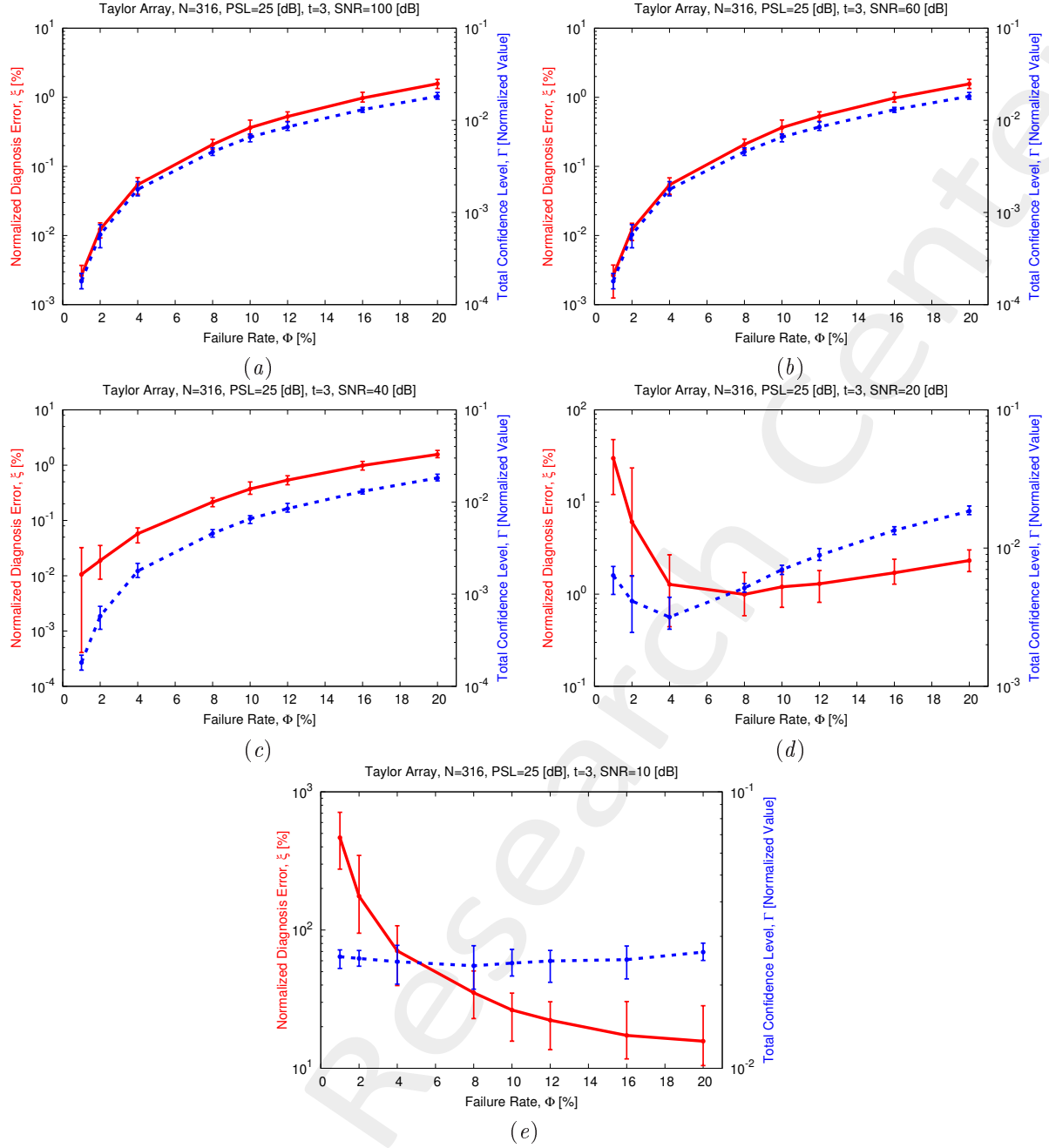


Figure 16: Taylor Array ($N = 316$, $PSL = 25$ [dB], $t = 3$) - Behavior of the average, minimum and maximum diagnosis error (ξ) and total confidence level (Γ) versus the failure rate (Φ), for (a) $SNR = 100$ [dB], (b) $SNR = 60$ [dB], (c) $SNR = 40$ [dB], (d) $SNR = 20$ [dB], and (e) $SNR = 10$ [dB].

More information on the topics of this document can be found in the following list of references.

References

- [1] P. Rocca, G. Oliveri, R. J. Mailloux, and A. Massa, "Unconventional phased array architectures and design methodologies - A Review," *Proc. IEEE*, vol. 104, no. 3, pp. 544-560, Mar. 2016 (DOI: 10.1109/JPROC.2015.2512389).
- [2] G. Oliveri, G. Gottardi, F. Robol, A. Polo, L. Poli, M. Salucci, M. Chuan, C. Massagrande, P. Vinetti, M. Mattivi, R. Lombardi, and A. Massa, "Co-design of unconventional array architectures and antenna elements for 5G base stations," *IEEE Trans. Antennas Propag.*, vol. 65, no. 12, pp. 6752-6767, Dec. 2017 (DOI: 10.1109/TAP.2017.2738065).
- [3] G. Oliveri, P. Rocca, and A. Massa, "Reliable diagnosis of large linear arrays - a Bayesian compressive sensing approach," *IEEE Trans. Antennas Propag.*, vol. 60, no. 10, pp. 4627-4636, Oct. 2012 (DOI: 10.1109/TAP.2012.2207344).
- [4] M. Salucci, A. Gelmini, G. Oliveri, and A. Massa, "Planar arrays diagnosis by means of an advanced Bayesian compressive processing," *IEEE Trans. Antennas Propag.*, vol. 66, no. 11, pp. 5892-5906, Nov. 2018 (DOI: 10.1109/TAP.2018.2866534).
- [5] A. Massa, P. Rocca, and G. Oliveri, "Compressive sensing in electromagnetics - A review," *IEEE Antennas Propag. Mag.*, pp. 224-238, vol. 57, no. 1, Feb. 2015 (DOI: 10.1109/MAP.2015.2397092).
- [6] G. Oliveri, M. Salucci, N. Anselmi, and A. Massa, "Compressive sensing as applied to inverse problems for imaging: theory, applications, current trends, and open challenges," *IEEE Antennas Propag. Mag.*, vol. 59, no. 5, pp. 34-46, Oct. 2017 (DOI: 10.1109/MAP.2017.2731204).
- [7] P. Rocca, M. A. Hannan, M. Salucci, and A. Massa, "Single-snapshot DoA estimation in array antennas with mutual coupling through a multi-scaling Bayesian compressive sensing strategy," *IEEE Trans. Antennas Propag.*, vol. 65, no. 6, pp. 3203-3213, Jun. 2017 (DOI: 10.1109/TAP.2017.2684137).
- [8] M. Carlin, P. Rocca, G. Oliveri, F. Viani, and A. Massa, "Directions-of-arrival estimation through Bayesian Compressive Sensing strategies," *IEEE Trans. Antennas Propag.*, vol. 61, no. 7, pp. 3828-3838, Jul. 2013 (DOI: 10.1109/TAP.2013.2256093).
- [9] L. Poli, G. Oliveri, P. Rocca, M. Salucci, and A. Massa, "Long-distance WPT unconventional arrays synthesis," *J. Electromagn. Waves Appl.*, vol. 31, no. 14, pp. 1399-1420, Jul. 2017 (DOI: 10.1080/09205071.2017.1348998).
- [10] G. Oliveri, M. Salucci, and A. Massa, "Synthesis of modular contiguously clustered linear arrays through a sparseness-regularized solver," *IEEE Trans. Antennas Propag.*, vol. 64, no. 10, pp. 4277-4287, Oct. 2016 (DOI: DOI: 10.1109/TAP.2016.2595623).

-
- [11] G. Oliveri and A. Massa, “Bayesian compressive sampling for pattern synthesis with maximally sparse non-uniform linear arrays,” *IEEE Trans. Antennas Propag.*, vol. 59, no. 2, pp. 467-481, Feb. 2011 (DOI: 10.1109/TAP.2010.2096400).
- [12] N. Anselmi, G. Oliveri, M. A. Hannan, M. Salucci, and A. Massa, “Color compressive sensing imaging of arbitrary-shaped scatterers,” *IEEE Trans. Microw. Theory Techn.*, vol. 65, no. 6, pp. 1986-1999, Jun. 2017 (DOI: 10.1109/TMTT.2016.2645570).
- [13] N. Anselmi, G. Oliveri, M. Salucci, and A. Massa, “Wavelet-based compressive imaging of sparse targets,” *IEEE Trans. Antennas Propag.*, vol. 63, no. 11, pp. 4889-4900, Nov. 2015 (DOI: 10.1109/TAP.2015.2444423).
- [14] L. Poli, G. Oliveri, F. Viani, and A. Massa, “MT-BCS-based microwave imaging approach through minimum-norm current expansion,” *IEEE Trans. Antennas Propag.*, vol. 61, no. 9, pp. 4722-4732, Sep. 2013 (DOI: 10.1109/TAP.2013.2265254).
- [15] G. Oliveri, N. Anselmi, and A. Massa, “Compressive sensing imaging of non-sparse 2D scatterers by a total-variation approach within the Born approximation,” *IEEE Trans. Antennas Propag.*, vol. 62, no. 10, pp. 5157-5170, Oct. 2014 (DOI: 10.1109/TAP.2014.2344673).
- [16] L. Poli, G. Oliveri, and A. Massa, “Imaging sparse metallic cylinders through a local shape function bayesian compressive sensing approach,” *J. Opt. Soc. Am. A*, vol. 30, no. 6, pp. 1261-1272, 2013 (DOI: 10.1364/JOSAA.30.001261).
- [17] L. Poli, G. Oliveri, P. Rocca, and A. Massa, “Bayesian compressive sensing approaches for the reconstruction of two-dimensional sparse scatterers under TE illumination,” *IEEE Trans. Geosci. Remote Sens.*, vol. 51, no. 5, pp. 2920-2936, May 2013 (DOI: 10.1109/TGRS.2012.2218613).
- [18] L. Poli, G. Oliveri, and A. Massa, “Microwave imaging within the first-order Born approximation by means of the contrast-field Bayesian compressive sensing,” *IEEE Trans. Antennas Propag.*, vol. 60, no. 6, pp. 2865-2879, Jun. 2012 (DOI: 10.1109/TAP.2012.2194676).
- [19] G. Oliveri, L. Poli, P. Rocca, and A. Massa, “Bayesian compressive optical imaging within the Rytov approximation,” *Opt. Lett.*, vol. 37, no. 10, pp. 1760-1762, 2012 (10.1364/OL.37.001760).
- [20] G. Oliveri, P. Rocca, and A. Massa, “A Bayesian compressive sampling-based inversion for imaging sparse scatterers,” *IEEE Trans. Geosci. Remote Sens.*, vol. 49, no. 10, pp. 3993-4006, Oct. 2011 (DOI: 10.1109/TGRS.2011.2128329).
- [21] N. Anselmi, L. Poli, G. Oliveri, and A. Massa, “Iterative multi-resolution bayesian CS for microwave imaging,” *IEEE Trans. Antennas Propag.*, vol. 66, no. 7, pp. 3665-3677, Jul. 2018 (DOI: 10.1109/TAP.2018.2826574).
- [22] L. Poli, P. Rocca, G. Oliveri, and A. Massa, “Failure correction in time-modulated linear arrays,” *IET Radar Sonar Navig.*, vol. 8, no. 3, pp. 195-201, 2014 (DOI: 10.1049/iet-rsn.2013.0027).